In situ nanoparticle-induced anti-oxidation mechanisms: Application to FeCrB alloys

Gaopeng Xu, Kui Wang, Haonan Li, Jiang Ju, Xianping Dong, Haiyan Jiang, Qudong Wang, Wenjiang Ding

PII: S0010-938X(21)00422-4

DOI: https://doi.org/10.1016/j.corsci.2021.109656

Reference: CS 109656

To appear in: *Corrosion Science*

Received Date: 20 January 2021

Revised Date: 27 May 2021

Accepted Date: 27 June 2021

Please cite this article as: { doi: https://doi.org/

In situ nanoparticle-induced anti-oxidation mechanisms: application to FeCrB alloys

Gaopeng Xu [a], Kui Wang [a,*], Haonan Li [a], Jiang Ju [b], Xianping Dong [b], Haiyan Jiang [a,*], Qudong Wang [a] and Wenjiang Ding [a]

[a] *National Engineering Research Center of Light Alloy Net Forming and State Key Laboratory of Metal Matrix Composites, Shanghai Jiao Tong University, 200240, Shanghai, P.R. China.*
[b] *School of Materials Science and Engineering, Shanghai Jiao Tong University, 200240, Shanghai, P.R. China.*

* Corresponding authors. 1
E-mail addresses: fateratory@sjtu.edu.cn (Kui Wang), jianghy@sjtu.edu.cn (Haiyan Jiang).

Highlights：

- *In situ* NPs significantly improve the oxidation resistance of FeCrB alloys.
- NPs facilitate the formation of a continuous and dense Cr_2O_3 protective film and enhance the adhesion of the oxide layers.
- NP assembly on the surface of borides can greatly reduce the growth rate of oxide layers.
- *In situ* NP-induced oxidation control that is firstly proposed may address the inherent deficiencies of conventional alloying.

Abstract:

In this work, *in situ* nanoparticles (TiB_2 and TiC) can be demonstrated to induce significant improvement in the oxidation resistance of Fe-12wt.%Cr-3.5wt.%B alloys. To unravel the roles of nanoparticles in the anti-oxidation of Fe-12wt.%Cr-3.5wt.%B alloys, samples with various nanoparticle contents were synthesized to investigate their oxidation resistance. Results show that nanoparticles facilitate the formation of a continuous and dense Cr_2O_3 protective film and enhance its adhesion with the matrix.

Furthermore, the nanoparticle assembly on the surface of borides can inhibit the inward diffusion of oxygen ions and the outward diffusion of cations, thereby effectively controlling the growth of oxide scales.

Key words: High temperature oxidation; *In situ* nanoparticle; oxide scale; TEM; FeCrB alloys.

1. Introduction

In the past few decades, many efforts have been made to improve the high-temperature corrosion-wear behaviors of metal materials in metal liquids during the liquid metal forming [1-4]. It is well documented that Fe-B alloys have a favorable corrosion-wear resistance thanks to a large quantity of stable and continuous borides formed in the matrix [5-12]. Nevertheless, borides tend to be oxidized to form B_2O_3 with a low melting point of 450 °C at high temperature [13], and B_2O_3 has a strong hygroscopicity to form volatile HBO_2 by the formation of B-O-H bonds with H_2O in air [14,15]. In this case, the volatilization of B_2O_3 may give rise to some pores in the matrix [16-18], which are considered as the fast channels for the diffusion of oxygen ions into the matrix, thus leading to a poor oxidation resistance of Fe-B alloys.

Although conventional alloying treatment is usually deemed as a simple and effective route for inhibiting the oxidation degradation of alloys. Several problems still remain in the alloying treatment. Firstly, it is well-established that the addition of Cr or Al can improve the oxidation resistance. The formed Cr_2O_3 and Al_2O_3 are usually regarded as the optimal protective oxides because the diffusion through them is relatively slow in comparison with most other oxides [19,20]. However, the formation of dense and continuous Cr_2O_3 or Al_2O_3 scale on the surface demands high concentration of Cr or Al, respectively [19,21-23]. The excessive Cr addition would adversely affect the size and morphology of borides, e.g. the formation of coarse lath-like primary borides, compromising the corrosion resistance and mechanical properties of Fe-B alloys [24,25]. Similarly, with excessive Al addition, the brittle and unstable Fe-Al intermetallic compounds (IMCs) would be formed in the matrix, which tend to be corroded by the liquid aluminum [26], and their exfoliation and dissolution eventually lead to the degradation of Fe-B alloys. Furthermore, the exposure environmental changes or stresses accompanying scale growth can give rise to the loss of adhesion and even spallation of oxides [27]. Even though investigations

[21,28-34] have shown that the addition of rare earth elements especially their corresponding stable oxides can cause a marked improvement in the adhesion of oxide scale, two key problems will emerge when it comes to rare earth elements and their oxides. One is that these incorporated rare earth oxide particles are inclined to agglomerate in the melt, thus impairing the "rare earth effect" [35]. The other is that rare earth resources are extremely scarce and relatively expensive [36], thus limiting their large-scale application in steel production. Hence, it is crucial to devise an alternative strategy or approach to break through the intrinsic deficiencies of conventional alloying treatment.

Nowadays, a number of studies [37-44] have demonstrated that the incorporation of ceramic particles with high strength, hardness, thermal and chemical stability are capable of imparting the enhanced oxidation resistance to alloys. It is reported that the introduction of TiC particles can significantly improve the oxidation resistance of 304 stainless steels [39,41,43]. During oxidation, TiO_2 particles oxidized from TiC particles on the surface of the alloy can promote the formation of Cr_2O_3 oxide scale while improving their adhesion with the matrix via the preformed TiO_2 pegging effect [38,41]. Nevertheless, the sizes of the added TiC particles in these studies are usually micrometer-scale, and few studies give attention to the influences of nanometer-scale particles on the oxidation resistance of alloys. Additionally, even though the improvement of surface oxide scale can be obtained upon addition of these microparticles (MPs), they usually show little or no contribution to the internal oxidation control of the matrix, especially for the alloys containing the intermetallics that are readily oxidized, e.g. the borides in FeCrB alloys. Consequently, the addition of MPs may fail to suppress the internal oxidation of borides in FeCrB alloys.

Until recently, Lee et al. [39] found that the stainless steels with finer TiC particle (1 μm) addition enjoys a better oxidation resistance than that with the size of 3 μm when investigating the effect of TiC particle size on the oxidation reistance of 304 stainless steel. Thereby, it could be expected that nanoparticles (NPs) might act as a more promising candidate than MPs. Moreover, according to our previous studies [3,45,46], the Ti element added to FeCrB alloys would react with B and C elements to form *in situ* TiB_2 and TiC NPs. Driven by a reduction in interfacial energy, these *in situ* NPs would assemble onto the surface of the boride to form a NP-layer, impeding the inward diffusion of oxygen ions and the outward diffusion of cations. Therefore, *in situ* NP-induced oxidation control may provide a potential avenue for improving the oxidation resistance of alloys and overcome the intrinsic limitations of conventional

alloying treatment.

In this work, the *in situ* NP-induced oxidation control is firstly employed to FeCrB alloys, which is expected to significantly improve their oxidation resistance. To unravel the roles of NPs (TiB_2 and TiC) in anti-oxidation behavior of FeCrB alloys, samples with various NP contents were synthesized to investigate their oxidation resistance in air at 750 °C for up to 200 h. Combined with the analysis of microstructure and thermodynamics as well as oxidation kinetics of the oxide scales formed on the alloy surface, the NP-induced anti-oxidation mechanisms are firstly proposed to further elucidate the oxide behavior of FeCrB alloys at elevated temperature, which may shed new light on the development of materials with excellent high temperature oxidation resistance.

2. Materials and methods

The Fe-Cr-B-(Ti) alloys were fabricated by a medium frequency induction furnace and cast as ingots with the dimension of 200×150×20 mm^3. The nominal chemical compositions (wt.%) of prepared Fe-Cr-B-(Ti) alloys named as JDF alloys were measured by inductively couple plasma atomic emission spectroscopy (ICP-AES) and presented in Table 1. Samples with the dimension of 5×5×6 mm^3 for isothermal oxidation tests were cut from the ingots with wire electrode cutting machine. Each surface was ground with SiC water-abrasive papers to remove surface oxidation skin and machining marks, ultrasonically cleaned with ethanol and dried. All the samples were placed in a roasted crucible (dried at 800 °C) in order to avoid weight loss due to exfoliation. High-temperature oxidation tests were conducted in air at 750 °C for 0-200 h, followed by air cooling. A box-type muffle furnace was adopted to perform the oxidation tests. The weight change of samples was weighed before and after the oxidation tests using an analytical balance with an accuracy of 0.01mg in order to investigate the oxidation kinetics. To minimize the experimental errors, three groups of parallel experiments were performed simultaneously.

The as-cast microstructure and the surface morphologies of oxidized samples were observed by scanning electron microscopy (SEM; JEOL JSM-7800F Prime). The oxide scales for 200 h were identified with X-ray diffraction (XRD; Smart Lab, Japan) using Cu Kα1 radiation (λ-0.15418 nm) with a scanning mode of 2θ of 20-90º

and a step size of 0.2º and 1 s in each step. X-ray photoelectron spectroscopy (XPS) was employed using a Kratos Axis Ultra^{DLD} spectrometer with a monochromatic Al Ka excitation (1486.6 eV) to measure the composition of the oxide scale formed at initial stage. Time of Flight Secondary Ion Mass Spectrometry (TOF-SIMS IV, ION-TOF GmbH, Münster, Germany) in dual beam mode was conducted to clarify the oxide distribution at different depths of the oxidation layer. Elemental distribution and phases identification in different regions on the cross-section of oxide scale was characterized using the scanning electron microscopy (SEM; MIRA3, Czech) equipped with the energy dispersive spectroscope (EDS; Aztec X-MaxN80) and electron backscattered diffraction (EBSD; Aztec Nordlys Max3), and scanning transmission electron microscopy (STEM, FEI Talos F200X G2) with EDS (FEI SuperX G2). High-resolution transmission electron microscope (HRTEM) analysis for the oxide scale was examined by the FEI Talos F200X microscope, operated at 200 kV acceleration voltage. TEM foils for observation of the oxide scales were fabricated with a focused ion beam (FIB; GAIA3). The elastic modulus, E of the oxide layer on the surface of JDF1 and JDF3 alloys were evaluated using Agilent Nano Indenter G200 at a constant load rate of 200 μN/s up to a pre-set peak value 500 mN with the Berkovich diamond indenter. Each test result is an average of five readings.

To gain microscopic insights into the atomic structure of the interface, the first-principles calculations based on Density Functional Theory (DFT) were performed using the Cambridge Serial Total Energy Package (CASTEP) module with the ultrasoft pseudo-potential [47]. The exchange-correlation functional at the generalized gradient approximation (GGA) level was described using the Perdew-Burke-Ernzerhof for solids (PBEsol) functional, which greatly improves the accuracy of PBE for equilibrium properties such as bond length [48,49]. The Kohn-Sham wave functions of the valence electrons were described by a plane-wave basis set with an energy cut-off of 400 eV. The Broyden-Fletcher-Goldfarb-Shanno (BFGS) scheme was chosen as the minimization algorithm in the geometric optimization process [50]. The Monkhorst-Pack scheme K-points grid sampling was set as 3×1×1 for the irreducible Brillouin zone.

3. Results

3.1. Microstructure analysis of JDF alloys

JDF alloys are novel high-boron steel developed on the basis of FeCrB alloys, which exhibit excellent resistance to liquid aluminum corrosion and favourable

mechanical properties. Previous studies [3,45] indicated that the microstructure of JDF1 alloy is composed of M_2B-type borides (M=Fe or Cr), ferrite and carbides. From Figs. 1a-c, it is evident that the primary borides (Cr-rich Fe_2B) are significantly refined with increasing Ti content, and their morphological transformation from platelet-like to block-like occurs. Besides, Ti addition can give rise to the modification of eutectic borides (Cr-rich Fe_2B) from coarse needle-like to fine rod-like. The magnified view of the fine and dispersed eutectic borides in JDF3 alloy is presented in Fig. 1e. Furthermore, it is worth noting that the volume fraction of the *in situ* formed ceramic particles (TiB_2 and TiC [3,45]) is increased with the Ti addition level. Apart from micron-scale ceramic particles as shown in Figs. 1b-d, a large number of nano-scale ceramic particles are also distributed homogeneously in the matrix, whose size and morphology are shown in Fig. 1f. Combined with HRTEM analysis in Fig. 1g, they are identified as TiB_2 nanoparticles (Space group: P6/mmm, a=0.303 nm, c=0.323 nm). When the Ti addition is raised up to 2.1 wt.%, the coarsening of primary borides occurs with platelet-like primary borides prevailing in the matrix. Besides, the agglomeration of some particles occurs as illustrated in Fig. 1d. By comparison, JDF3 alloy has the finest and most homogeneous microstructure, as well as the highest number density of borides in the matrix [3,45].

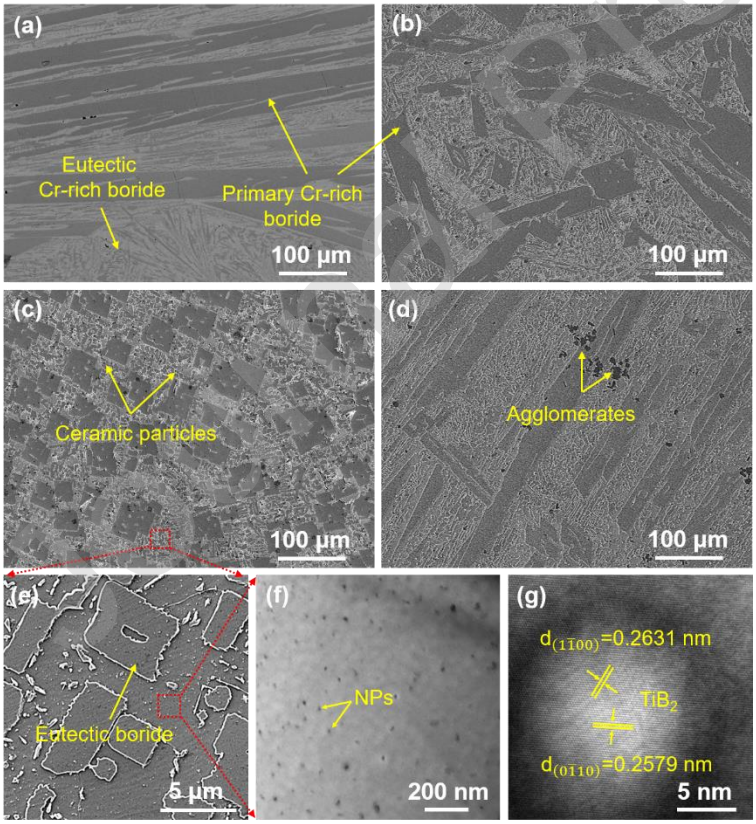

Fig. 1. Microstructures of JDF alloy: (a) JDF1 alloy; (b) JDF2 alloy; (c) JDF3 alloy; (d) JDF4

alloy; (e) Refined eutectic Cr-rich Fe_2B in JDF3 alloy; (f) NPs dispersed in matrix; (g) HRTEM image of a single TiB_2 nanoparticle.

3.2. Isothermal oxidation kinetics

The curves of oxidation kinetics of JDF alloys in air at 750 °C are plotted in Fig. 2a, in which the weight gain per unit area $\Delta W/A$ is the function of oxidation time t. Compared with JDF1 alloy, a pronounced improvement in oxidation resistance was achieved by JDF3 alloy. To analyze the oxidation kinetics of JDF alloys, the obtained experimental data was fitted by

$$\left(\frac{\Delta W}{A}\right)^n = k_p t \quad (1)$$

where ΔW is the weight gain (g), A is the surface area of the samples (m^2), n is an oxidation exponent (n = 1, linear relationship; n = 2, parabolic relationship), k_p is the rate constant of power function (g^n/m^{2n}), and t is the oxidation time (h). The fitted curves were plotted in Fig. 2a, and the n values corresponding to various JDF alloys were obtained and shown in Fig. 2b. The oxidation behavior of JDF alloys obeyed a parabolic growth kinetics ($n \approx 2$) from 0 to 200 h. Studies [31,51] show that the larger the value of n, the higher the compactness of the oxide scale. Hence, the oxide scale of JDF3 alloy can be deemed as the most complete and compact one in comparison with other JDF alloys. The oxidation kinetics of JDF alloys was further analyzed by the (weight gain per unit area)^n as function of oxidation time in Figs. 2c-f. The values of the slope k_p that is an indicator of the oxidation rate can be determined by linear fitting. The fitting results reveal that the oxidation constant of JDF3 is 0.114 $g^2m^{-4}h^{-1}$ much smaller than that of JDF1. Thus, it can be speculated that the enhanced high temperature oxidation resistance of JDF alloys appears to be attributable mainly to the *in situ* formed ceramic particles.

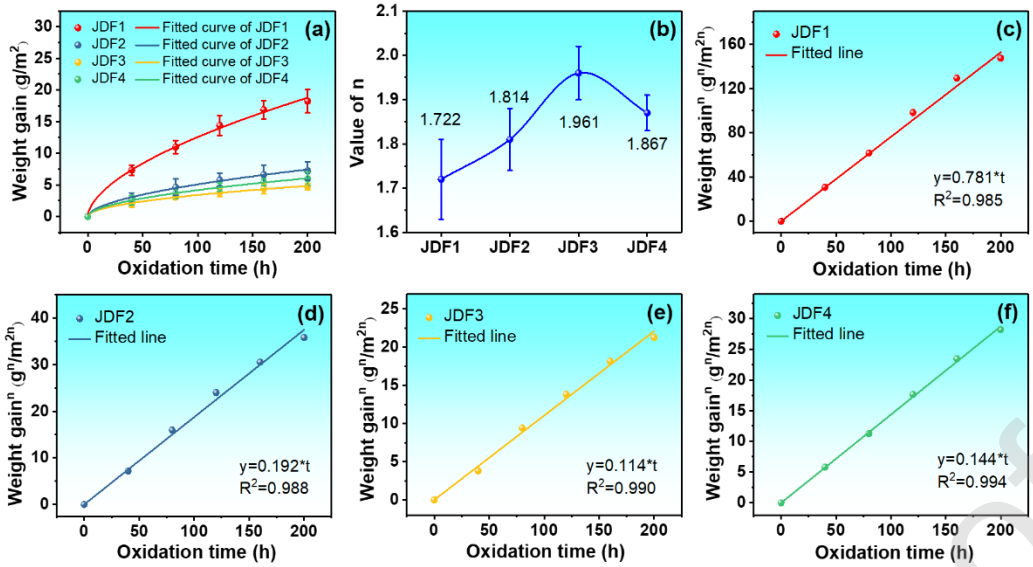

Fig. 2. (a) Oxidation kinetics of JDF alloys at 750 °C in air up to 200 h; (b) Oxidation exponent of JDF alloys; (c) JDF1 alloy; (d) JDF2 alloy; (e) JDF3 alloy; (f) JDF4 alloy.

3.3 Microstructure analysis of the oxide scale

The surface morphologies of the oxide scales of JDF1 and JDF3 alloys after oxidation in air at 750 °C for 2 h, 40 h and 200 h are shown in Fig. 3. At an initial stage of oxidation (2 h), a continuous oxide scale is formed rapidly on the surface of JDF1 alloy (Fig. 3a). The inset of Fig. 3a indicates that the oxide scale has a loose and porous structure with straw-like oxides embedded in it. Based on the EDS results, the oxide scale and straw-like oxides are enriched by Fe, O and a small amount of Cr. Combined with the XPS surveys and high-resolution spectra of the oxide surface (Figs. 4a), it can be inferred that the oxide scale consists of a mixture of Fe_3O_4, $FeCr_2O_4$ and Cr_2O_3 and the straw-like oxides may be Fe_2O_3 [22]. Unlike the JDF1 alloy, numerous oxide particles with pebble-like or spherical morphology are dispersed on the surface of JDF3 alloy as marked by the yellow arrows in Fig. 3b. According to the EDS analysis in Table 2 and the XPS surveys in Figs. 4b, the pebble-like and spherical oxides are likely to be SiO_2 and TiO_2, respectively. In addition, Cr_2O_3 scale is also found on the surface of the matrix and borides. After 40 h oxidation, several straw-like oxide nodules are formed on the surface of JDF1 alloy and some cracks can be also observed in the oxide scale as depicted in Fig. 3c. In stark contrast, the oxide scale of JDF3 alloy in Fig. 3d is still continuous and dense, and no pores or micro-cracks can be detected. When the oxidation time reaches up to 200 h, a large number of spalling zones, cracks and pores are formed on the surface of

JDF1, providing fast channels for the diffusion of oxygen ions and thus promoting the oxidation of JDF1 alloy. The analysis of EDS and XRD implies that the inner oxide at the spalling zone is composed of Fe_3O_4 (Space group: $Fd\bar{3}m$, a=0.8396 nm) while the surface straw-like oxide node is composed of Fe_2O_3 (Space group: $R\bar{3}c$, a=0.5036 nm, c=1.3749 nm). On the contrary, the oxide layer containing fine and compact Cr_2O_3 (Space group: $R\bar{3}c$, a=0.4959 nm, c=1.3594 nm) particles is formed on the surface of JDF3 alloy. The continuous and compact Cr_2O_3 oxide film could effectively inhibit the diffusion of oxygen ions into the matrix, leading to the enhanced oxidation resistance of JDF3 alloy.

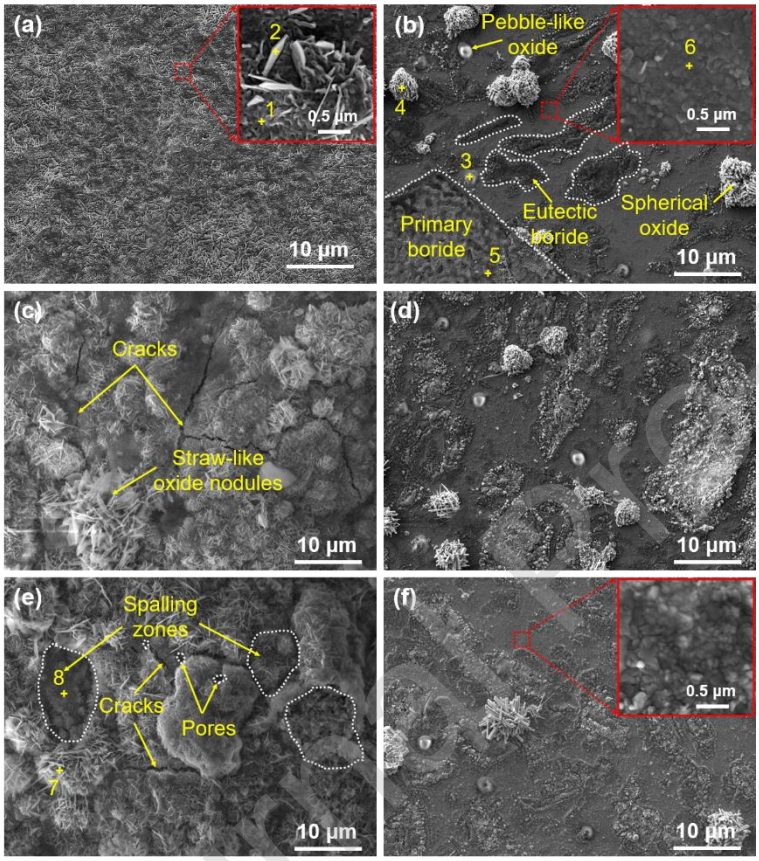

Fig. 3. Surface morphology of the JDF1 and JDF3 alloys oxidized in air at 750 °C: (a) 2 h, (c) 40 h, and (e) 200 h for JDF1 alloy; (b) 2 h, (d) 40 h, and (f) 200 h for JDF3 alloy.

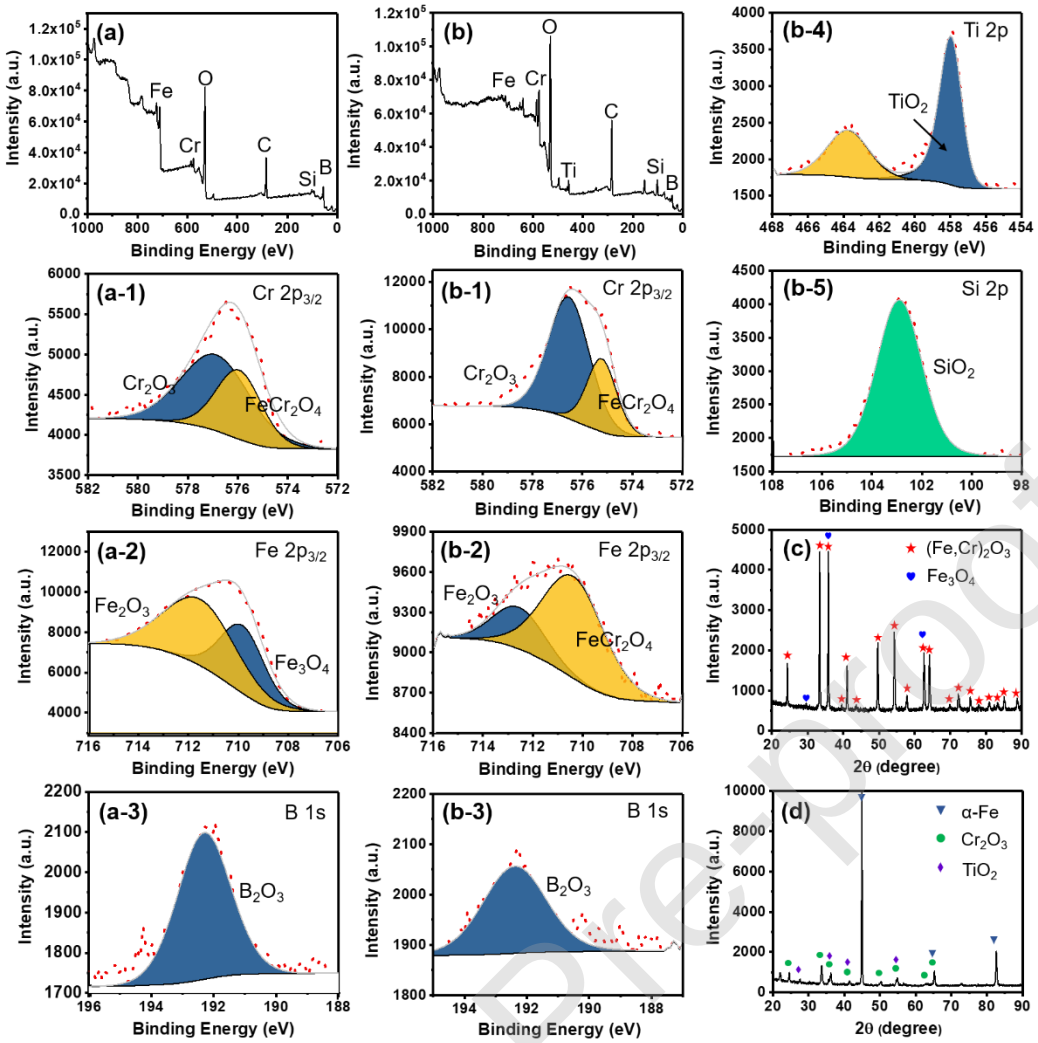

Fig. 4. (a) and (b) XPS core level spectra recorded for the oxidation scale formed at the surface of JDF1 and JDF3 alloy oxidized at 750 °C for 2 h, respectively; (c) and (d) XRD spectra of oxide scales in JDF1 and JDF3 alloy oxidized at 750 °C for 200 h, respectively.

In order to clarify the oxide scale structure, the cross-sectional morphology and corresponding EDS element mappings combined with EBSD analysis of JDF alloys are shown in Figs. 5 and 6. After exposed in air at 750 °C for 200 h, the formation of a bi-layered oxide scale with a porous structure occurs on the surface of JDF1 alloy (Fig. 5a). EDS mappings in Figs. 5b-g reveal that the outer oxide layer is rich in Fe and O other than a trace of Cr and Si. Combined with the XRD analysis, it is found that the outer oxide layer is a mixing layer primarily containing the loose Fe_3O_4 and $(Fe,Cr)_2O_3$. For the inner oxide layer, it can be observed that the Fe element gradually decreases while the Cr element increases from outside to inside. Some Si-rich oxides are distributed in the oxide layer. According to XRD and EDS mapping results, the

inner oxide layer is also a mixing oxide layer composed dominantly of Cr_2O_3, but also minor SiO_2 distributed in between them. As illustrated in Figs. 5h-k, the mixing oxide scale can be clearly divided into the outer coarse-grained layer and the inner fine-grained layer. Additionally, it is apparent from the element mappings of Si and B that a thin oxide layer rich in Si and B is formed at the interface between the matrix and the inner oxide layer. Lv et al. [16] suggested that it may be the B_2O_3-SiO_2 borosilicate that is capable of inhibiting the diffusion of oxygen ions into matrix to some extent. Yet, the formed borosilicate layer is not dense sufficiently with many pores and cracks existing in the layer as shown in Fig. 5a. Moreover, the newly-formed Cr_2O_3 oxides at later stage of oxidation would generate growth stress in the inner oxide layer, which could not be totally released by the outer coarse-grained layer, thus leading to the formation of cracks. As a consequence, the formation of pores and cracks in the oxide scale would result in the abysmal adhesion of the oxide scale to the matrix and therefore the deterioration of the oxidation resistance of JDF1 alloy.

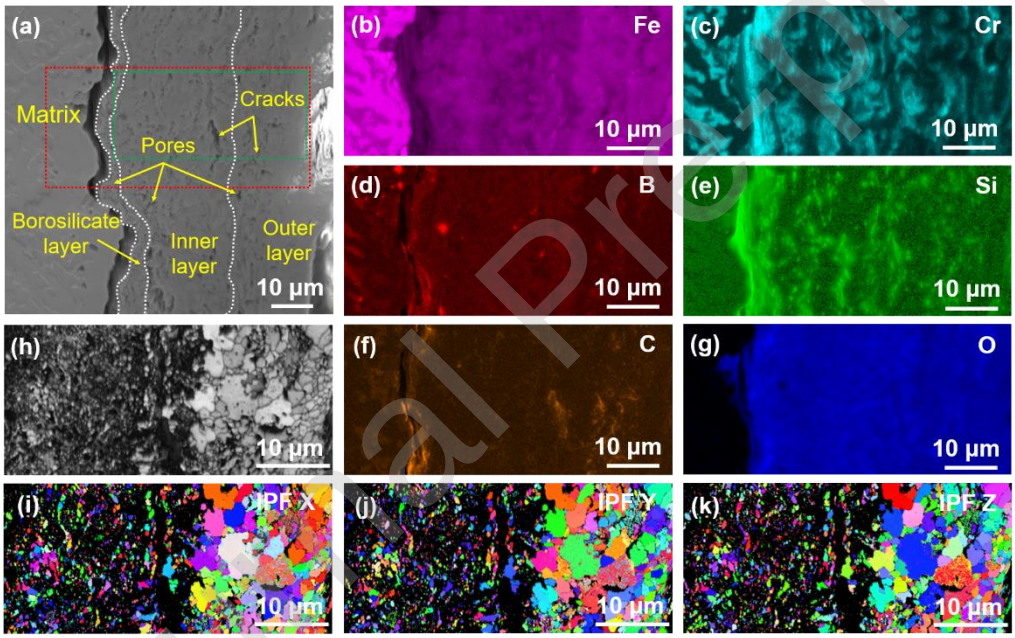

Fig. 5. Cross-sectional morphology of JDF1 alloy after 200 h of oxidation at 750 °C: (a) SEM micrograph; (b-g) Fe, Cr, B, Si, C and O elemental maps of surface oxide scale; (h) Pattern quality image; (i-k) IPF images of the surface oxide.

Compared with JDF1 alloy, the thickness of the oxide scale of JDF3 alloy is much smaller. To analyze the structure of oxide scales, TEM samples were prepared by FIB from the regions where the α-Fe matrix, primary borides and their corresponding oxide scales are distributed as shown in Fig. S2. Fig. 6a shows the bright field STEM

image of the oxide scale on the surface of α-Fe matrix (Region 1 in Fig. S2) after 200 h oxidation at 750 °C and the corresponding STEM-EDS elemental mappings. In general, the distribution of elements in the oxide scale is non-uniform as seen from Figs. 6a1-a6. Combined with the EDS line analysis results in Fig. 6c, the oxide scale can be divided into three sub-layers, i.e. the inner layer □, the intermediate layer □ and the outer layer □. Layer I and III are composed of Cr-rich oxides while layer II consists of Fe-rich oxides. Si- and Ti-rich oxides (corresponding to SiO_2 and TiO_2 according to XRD and XPS analysis) dispersed throughout the oxide scale are scattered and discontinuous. It is noteworthy that the Cr-rich oxide grains of the inner layer have an ultrafine equiaxial structure, whose average size is much smaller than that of the outer layer. In addition, compared with JDF1 alloy, the oxide layer of JDF3 alloy is more compact and the oxide grains especially in the inner oxide layer are more refined, which effectively enhances the plasticity of oxide scale. Moreover, according to the results of TEM and STEM-EDS mappings in Figs. 6a, some areas marked by yellow arrows, where are void and contain no element, can be observed in the oxide scale. Ju et al. [18] believed that these cavities are beneficial to release the stress generated during the growth of oxides.

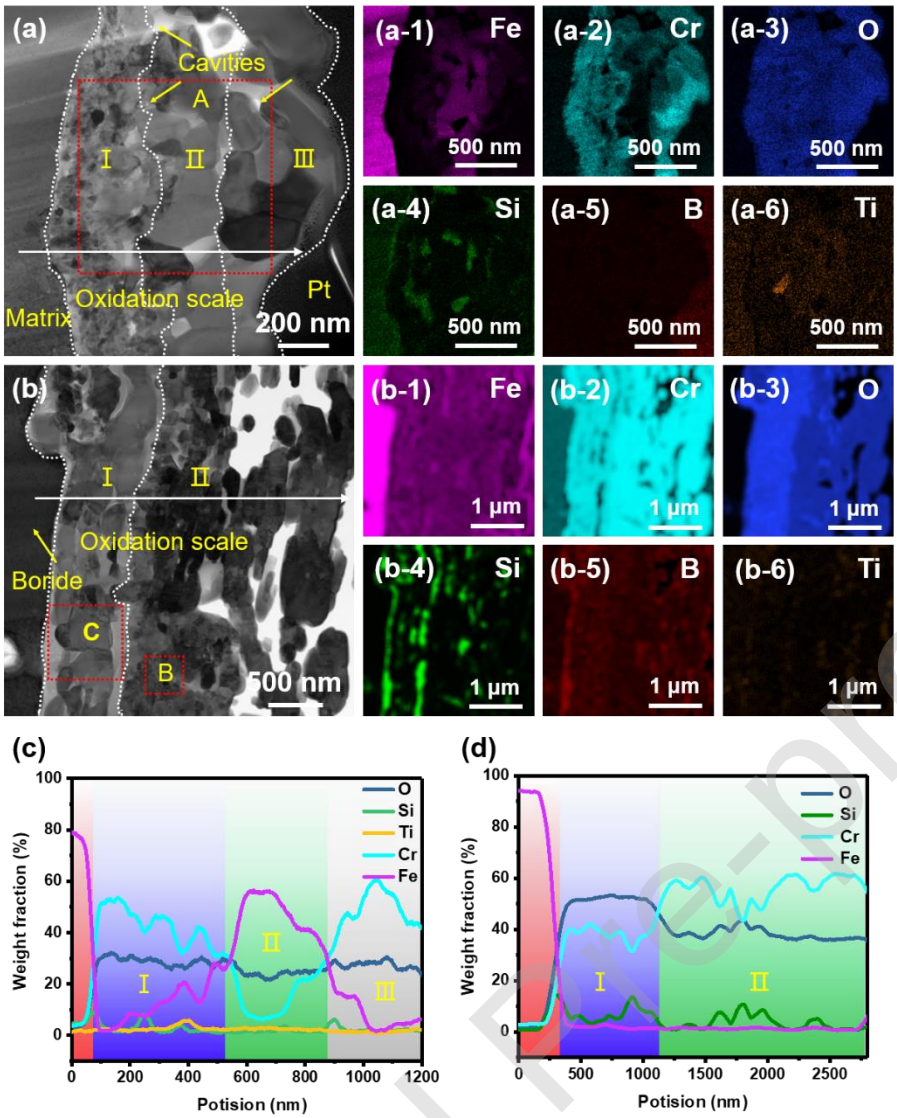

Fig. 6. JDF3 alloy after oxidation at 750 °C for 200 h: (a) Bright-field STEM image taken at the interface between the oxide scale and the matrix (corresponding to the Region 1 of Fig. S2); (a1)-(a6) STEM-EDS elemental mappings of Fe, Cr, O, Si, B, Ti, respectively; (b) Bright-field STEM image taken at the interface between the oxide scale and the boride (corresponding to the Region 2 of Fig. S2); (b1)-(b6) STEM-EDS elemental mappings of Fe, Cr, O, Si, B, Ti, respectively; (c) EDS line analysis results of the white line in Fig. 6a; (d) EDS line analysis results of the white line in Fig. 6b.

As shown in Fig. 6b, the oxidation degree of primary borides is higher than that of the matrix, and the thickness of oxide scale reaches 2.5 μm, which is 2 times than that of the oxide scale on the matrix. Based on the EDS mapping (Figs. 6b1-b6) and the EDS line analysis in Fig. 6d, the oxide scale on the surface of primary boride (Region

2 in Fig. S2) can be divided into two sub-layers, i.e. the inner Cr-rich layer I and the outer Cr-rich layer II. Similar to the oxide scale on the α-Fe matrix, Si-rich oxides are dispersed across the scale. However, continuous Si-rich oxide layers are formed at the inner oxide layer/outer oxide layer interface and the matrix/inner oxide layer interface. Intriguingly, the Si-rich oxide layer at the matrix/inner oxide layer interface coincides nicely with the distribution of B element, implying the formation of the B_2O_3-SiO_2 borosilicate layer. Different from the B_2O_3-SiO_2 borosilicate layer formed in JDF1 alloy, the one in JDF3 alloy is quite dense and continuous and able to more effectively inhibit the diffusion of oxygen ions into the primary boride. Additionally, the inner oxide layer containing Cr and Si-rich oxides is also complete and compact, offering a strong protective effect on the oxidation of primary borides in spite of their tendency to be oxidized.

To clarify the crystal structures and orientation relationships of oxides, HRTEM examination of the oxide layer was conducted in Fig. 7. Fig. 7a is the magnified TEM image corresponding to the red box area A in Fig. 6a. The Point 1 in the inner oxide layer, the Points 2-4 in the intermediate oxide layer and the Point 5 in the outer oxide layer were analyzed by HRTEM (Figs. 7b-f). The results demonstrate that the oxides corresponding to Points 1 to 5 are Cr_2O_3 (Space group: $R\bar{3}c$, a=0.4959 nm, c=1.3594 nm), $(Fe,Cr)_2O_3$ (Space group: $R\bar{3}c$, a=0.4997 nm, c=1.3621 nm), $FeCr_2O_4$ (Space group: $Fd\bar{3}m$, a=0.8379 nm), Fe_2O_3 (Space group: $R\bar{3}c$, a=0.5036 nm, c=1.3749 nm) and Cr_2O_3, respectively. It has been demonstrated that the inner and outer oxide layers are both composed of Cr_2O_3 while the intermediate oxide layer mainly contains Fe_2O_3, $(Fe,Cr)_2O_3$ and $FeCr_2O_4$. Actually, there are also SiO_2 and TiO_2 oxide particles distributed throughout the oxide scale as shown in Fig. 6. Researchers [22,38,39,41] speculated that SiO_2 or TiO_2 particles might act as nucleation sites to promote the formation and growth of Cr_2O_3. To verify it, the interfaces between SiO_2/TiO_2 and surrounding Cr_2O_3 that correspond to Zone a and b in Fig. 7a respectively were investigated by HRTEM analysis (Figs. 7g-i). Fig. 7g is the HRTEM image taken along the $[10\bar{5}\bar{5}\bar{9}]$ zone axis of Cr_2O_3. The concentric diffraction halo in Fig. 7g

indicates that the SiO_2 has an amorphous structure. It is evident that no crystallographic orientation relationship exists between SiO_2 and Cr_2O_3 and thus SiO_2 may not act as the heterogeneous nucleation site for Cr_2O_3. Furthermore, the HRTEM image of the interface between TiO_2 and Cr_2O_3 is given in Fig. 7h, in which a coherent and taintless interface can be observed. Combined with the FFT analysis of the interface in Fig. 7h, two parallel orientation relationships between TiO_2 and Cr_2O_3 can be obtained as $(020)_{TiO2}//(11\bar{2}0)_{Cr2O3}$, $[10\bar{2}]_{TiO2}//[\bar{2}201]_{Cr2O3}$; $(2\bar{1}1)_{TiO2}//(\bar{2}11\bar{6})_{Cr2O3}$, $[10\bar{2}]_{TiO2}//[\bar{2}201]_{Cr2O3}$. The atomically smooth and coherent interface indicates that TiO_2 particles may become the potential nucleation sites for Cr_2O_3 oxides to promote their heterogeneous nucleation.

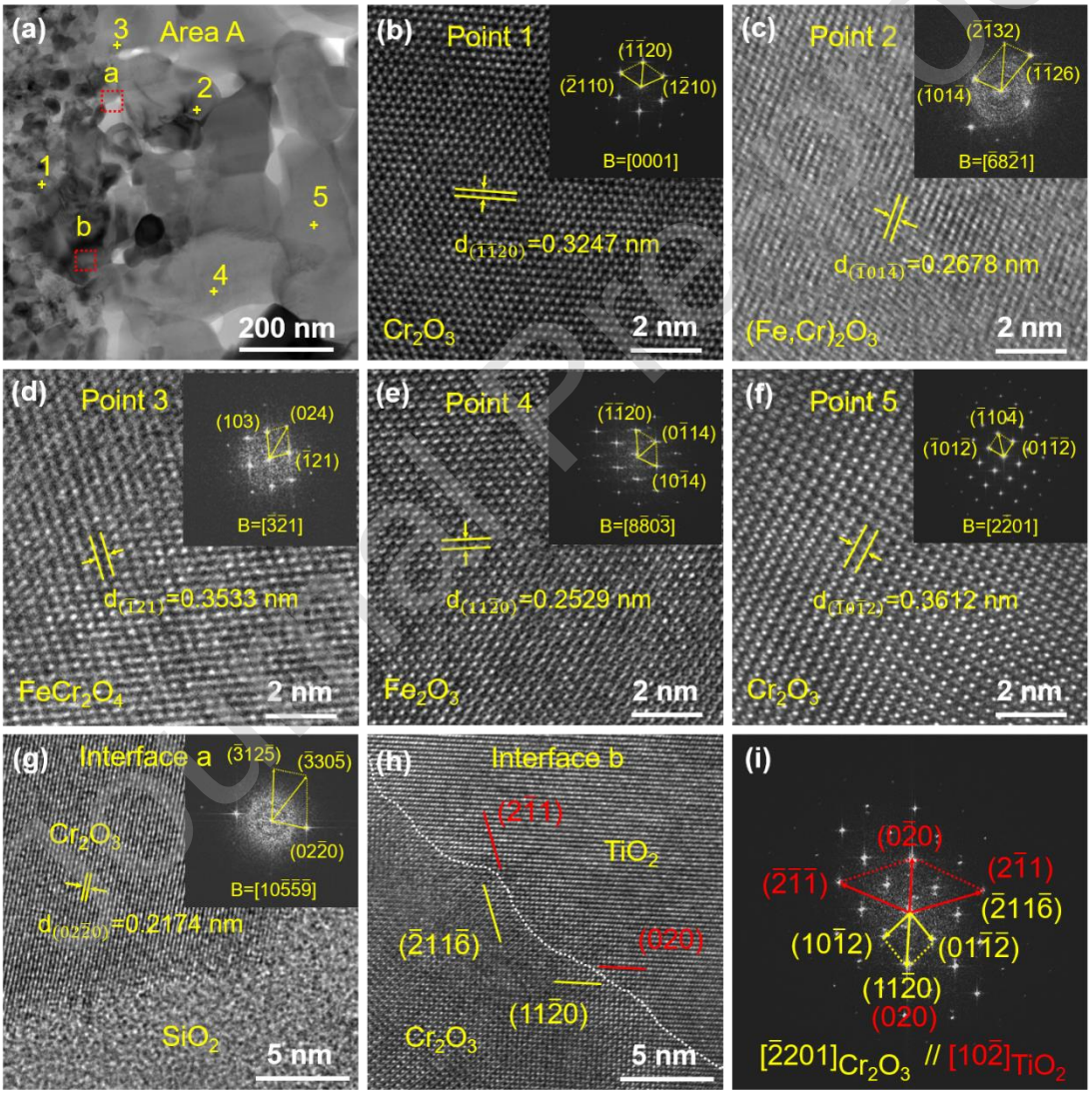

Fig. 7. (a) BF-TEM image of Area A in Fig. 6a; (b)-(f) HRTEM images corresponding to Points 1

to 5 in Fig. 7a, respectively; (g) and (i) HRTEM images corresponding to interface a and b in Fig. 7a, respectively; (i) FFT analysis of the interface between TiO_2 and Cr_2O_3; All the insets in Figs. 7b-g are the corresponding FFT analysis.

According to STEM-EDS results in Figs. 6b1-6, the outer oxide layer in Fig. 6b is a Cr-rich oxide layer containing some Si-rich oxide particles. Fig. 8a is the TEM image of the outer oxide layer (Area B in Fig. 6b) in which many fine oxide particles are distributed. Fig. 8b highlights the interfacial structure between the fine oxide particle and the Cr-rich oxide. Based on the crystallographic information provided in Figs. 8b1-2, they are likely to be TiO_2 and Cr_2O_3. It is also observed that a semi-coherent interface is formed between them and a pair of parallel orientation relationship (OR) can be attained as $(110)_{TiO2}//(01\bar{1}0)_{Cr2O3}$. The TEM image of the inner oxide layer (Area C in Fig. 6b) is also given in Fig. 8c. It can be seen that the size of oxide grains in the inner layer is much larger than that in the outer layer, and few fine oxide particles like TiO_2 is embedded in this layer. Fig. 8d displays the HRTEM analysis of the (Si,B)-rich oxide. The concentric diffraction halo indicates that the (Si,B)-rich oxide in inner oxide layer is an amorphous B_2O_3-SiO_2 glass. Fig. 8e is the HRTEM analysis of Point 7 in Fig. 8c. Results further confirm that the inner oxide layer is mainly composed of Cr_2O_3.

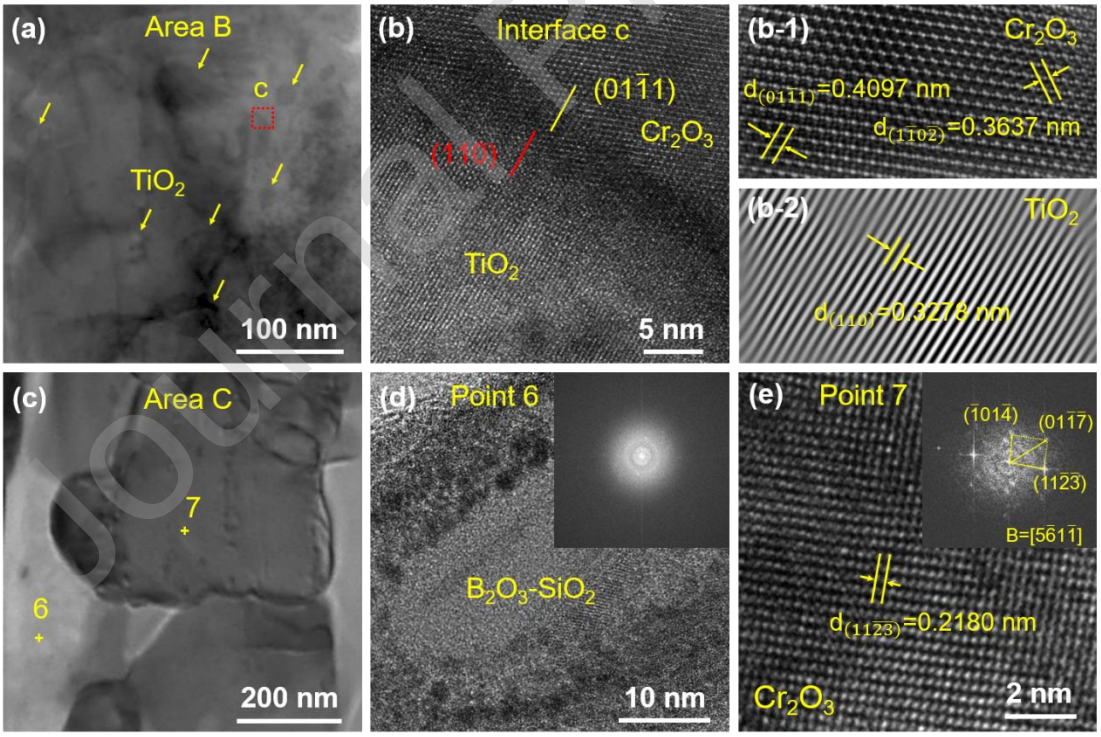

Fig. 8. (a) BF-TEM image of Area B in Fig. 6a; (b) HRTEM image corresponding to interface c in Fig. 8a; (b-1) IFFT of Cr_2O_3 in Fig. 8b; (b-2) IFFT of TiO_2 in Fig. 8b; (c) BF-TEM image of Area

C in Fig. 6a; (d) HRTEM image corresponding to Point 6 in Fig. 8c, the inset is the corresponding FFT image of Fig. 8d; (e) HRTEM image corresponding to Point 7 in Fig. 8c, and the inset is the corresponding FFT image of Fig. 8e.

As shown in Fig. 6c, the oxide contents vary wildly along the direction perpendicular to the surface from outside to inside. The EDS line analysis suggests that three separate oxide layers can be determined based on the depths from the surface to the matrix, i.e. the outer layer (0-300 nm), the intermediate layer (300-700 nm) and the inner layer (700-1100 nm). Given the information provided by 2D micrographs may not be used to evaluate the 3D spatial distribution of oxides, TOF-SIMS 3D chemical analysis is performed to visualize the spatial distribution of phases in oxide layers. As indicated in Fig. 9, TOF-SIMS 3D chemical maps of CrO^-, FeO^-, SiO^-, TiO^- and BO^- secondary ions are shown in the depths ranging from the outer layer (90-110 nm) to the intermediate layer (390-410 nm) to the inner layer (790-810 nm). The results manifest a significant discrepancy in the oxide contents and distribution for the JDF3 alloy in different depths. For the outer layer with 90-110 nm depth, a strong yellow signal of CrO^- can be detected. Thus, a large amount of CrO^- is uniformly distributed in the outer layer. Other oxides including SiO^-, TiO^- and BO^- can also be observed in the outer layer, showing an inhomogeneous lateral distribution. For the intermediate layer with 390-410 nm depth, CrO^- and FeO^- are distributed homogeneously, while SiO^-, TiO^- and BO^- are segregated locally. Compared with CrO^-, FeO^- exhibits a stronger enrichment in the intermediate layer. Similarly to the outer layer, the enrichment of CrO^- and segregation of SiO^-, TiO^- and BO^- also occur in the inner layer with 790-810 depth. The TOF-SIMS 3D chemical analysis further confirms that the compositions of oxide layers are not homogeneous: the outer and inner oxide layers are mainly composed of Cr-rich oxides, and the intermediate oxide layer mainly contains Fe-rich oxides, which is consistent with the STEM results. For a systematic overview of the characteristics of different oxide layers, 3D renderings of CrO^- in outer layer, FeO^- in intermediate layer and CrO^- in inner layer are presented in Fig. 9. Combined with the STEM analysis, the oxide layer can be divided specifically into the outer fine-grained Cr-rich oxide layer, intermediate fine-grained Fe-rich oxide layer and inner ultrafine-grained Cr-rich oxide layer.

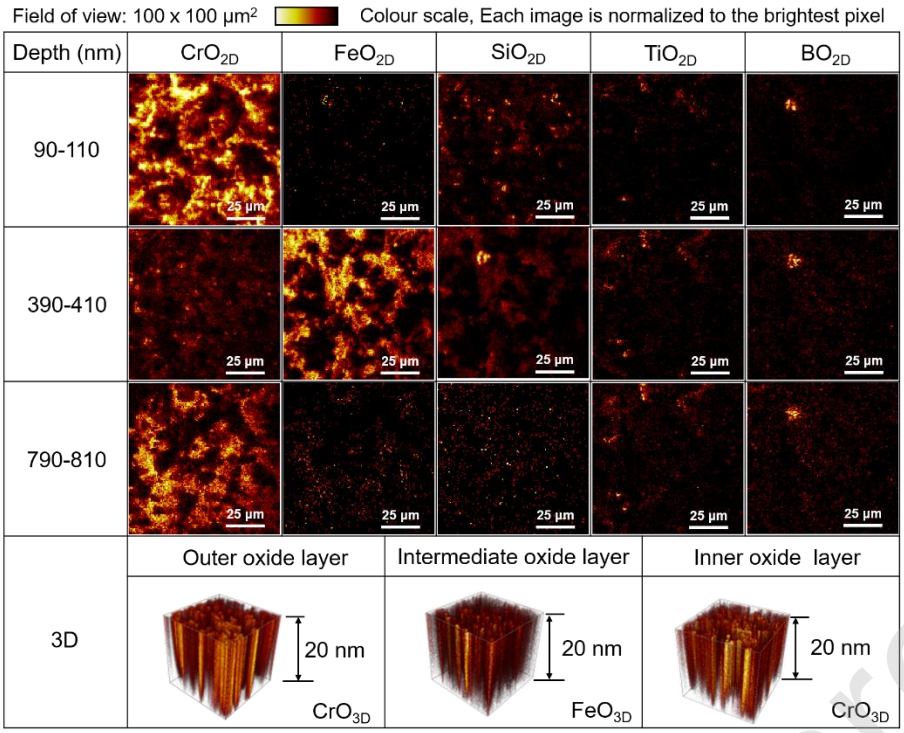

Fig. 9. TOF-SIMS negative ion images of CrO^-, FeO^-, SiO^-, TiO^- and BO^- recorded for the surface of JDF3 alloy at different depths.

4. Discussion

4.1. Thermodynamics and kinetics analysis of oxidation

At the initial stage of oxidation, the formation probability of oxides can be analyzed via the affinity to oxygen. The change of Gibbs free energy (ΔG) and the equilibrium partial pressures of oxygen (P_{O_2}) during the formation of reaction products can be calculated by HSC Chemistry 6.0 and listed in Table 3. All values of ΔG for reactions are found to be negative at 750 °C and the equilibrium partial pressures of oxides are lower than the actual oxygen partial pressure in the furnace, providing rationale to understand their formation. It is well-documented that the more negative the ΔG value and the lower the P_{O_2} value, the more readily the oxide is formed. Hence, the alloying elements are preferentially oxidized following the sequence: Ti > Si > B > Cr > Fe. Note that the oxidation of multicomponent alloys is not only affected by thermodynamics but also by growth kinetics [52]. As shown in Fig. 2a, all JDF alloys basically obey a parabolic law. It can be inferred that the diffusion process is the rate-limiting step for the growth of oxide layer as the parabolic law is derived from Fick's first law of diffusion. Therefore, the relationship between the diffusion coefficient D

and the temperature T can be given by

$$D=D_0\cdot\exp(\frac{-Q}{RT}) \quad (2)$$

where D_0 is the vibration frequency factor (m^2/s), Q is the diffusion activation energy (kJ/mol), R is the gas constant of 8.314 (J/(mol·K)), and T is the oxidation temperature (K). From Table 4, it can be found that the diffusion coefficient of B element in the matrix is four orders of magnitude higher than that of other elements. Although the diffusion coefficients of Fe, Cr, Si, and Ti are of the same order of magnitude, the diffusion coefficient of Si is 4 times higher than that of Cr, 5 times higher than that of Fe and 8 times higher than that of Ti. In principle, the growth of oxides is controlled by the outward diffusion of cations and inward diffusion of anions. In this case, P_{O_2}, oxidation temperature, and chemical composition are the three critical factors affecting the growth of oxide layer [53]. In this work, ceramic particles (TiB_2 and TiC) with various contents are *in situ* formed in the matrix of JDF alloys by tuning the addition level of Ti element. These titaniferous ceramic particles would have a significant effect on the diffusion behavior of alloying elements, the formation of oxide layers and the oxidation behavior of JDF alloys.

4.2. *In situ* nanoparticle-induced anti-oxidation of FeCrB alloys

4.2.1. Heterogeneous nucleation of Cr_2O_3 oxide

Titaniferous ceramic particles in JDF3 alloy, especially the nanoscale TiB_2 and TiC, are preferentially oxidized to form fine TiO_2 particles at high temperatures thanks to the low Gibbs free energy (Table 3). Chen et al. [38] and Wu et al. [41] speculated that the oxidized TiO_2 particles can act as nucleation sites for Cr_2O_3 to promote their heterogeneous nucleation and thus facilitate the establishment of Cr_2O_3 film, although no strong evidence was provided to confirm their arguments. In this work, Cr_2O_3 is directly observed to form three coherent interfaces with TiO_2 as shown in Fig. 7h and 8b. According to the lattice mismatch theory [58], the disregistries of three interfaces are calculated and listed in Table 5. Theoretically, if the lattice mismatch is less than 6.0%, it can be considered as the effective heterogeneous nucleant. The calculated results show that Cr_2O_3 may nucleate heterogeneously on the (110), (020) and $(2\bar{1}1)$ planes of TiO_2.

To better understand the nature of the interfaces between Cr_2O_3 and TiO_2, a DFT theoretical analysis has been conducted based on the interface structure, the interfacial

bonding energy and the work of adhesion. The coherent orientation relationships between TiO_2 and Cr_2O_3 are listed in Table 5, including $(2\bar{1}1)_{TiO2}//(\bar{2}11\bar{6})_{Cr2O3}$, $(020)_{TiO2}//(11\bar{2}0)_{Cr2O3}$ and $(110)_{TiO2}//(01\bar{1}0)_{Cr2O3}$ interfaces, in which the coherent planes are matched across the interface.

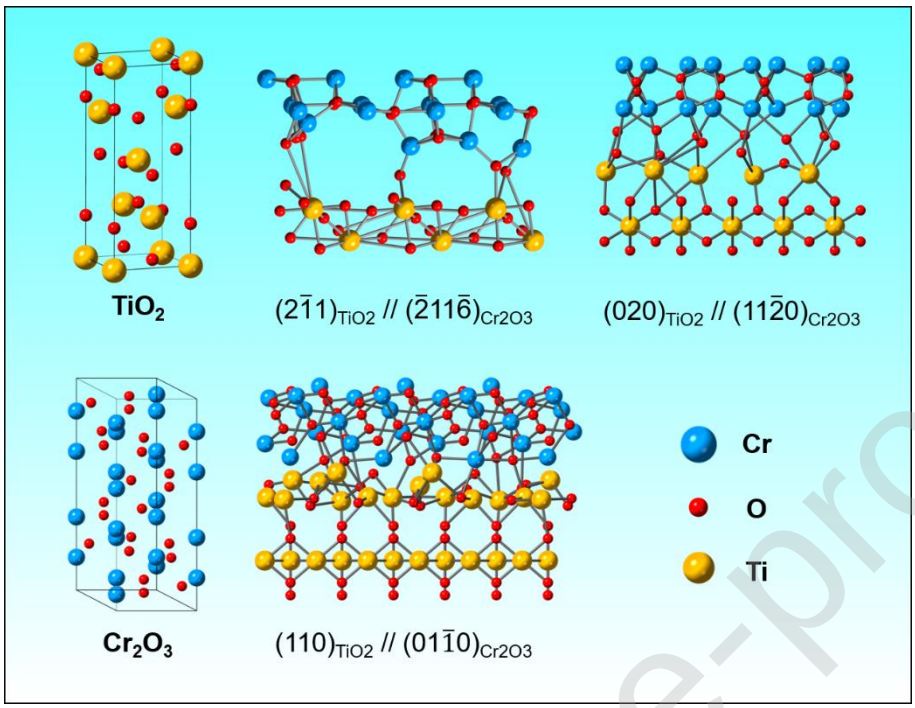

Fig. 10. Interface structure of TiO_2 and Cr_2O_3

The interfacial energy is an important measure of interfacial stability, which can be defined as

$$E_{ad}=E_{Cr_2O_3/TiO_2}-(E_{Cr_2O_3}+E_{TiO_2}) \quad (3)$$

where E_{ad} is the interfacial energy, E_{Cr2O3} and E_{TiO2} are the total energy of the relaxed, isolated Cr_2O_3 and TiO_2 slabs in the same supercell when one of the slabs is kept and the other one is replaced by vacuum, respectively, and $E_{Cr2O3/TiO2}$ is the total energy of the Cr_2O_3/TiO_2 interface system. Generally, the lower the interfacial energy, the more stable the interface structure. In this work, the interfacial energies of the three interfaces are all negative as shown in Table 5. Among them, the interface between $(2\bar{1}1)_{TiO2}$ and $(\bar{2}11\bar{6})_{Cr2O3}$ planes has the minimum interfacial energy and is the most stable.

The ideal work of adhesion (W_{ad}), which is defined as the reversible work required to separate the interface into two free surfaces, is commonly utilized to describe the interfacial adhesion strength [59]. It can be determined by the difference in total energy between the interface and its isolated slabs:

$$W_{ad} = (E_{Cr_2O_3}+E_{TiO_2}-E_{Cr_2O_3/TiO_2})/S \quad (4)$$

where S is the interface area. By this definition, a stronger interface would have a more positive work of adhesion value. Table 5 shows the calculated W_{ad} for the three interface structures, and all the values are positive. By comparison, the $(2\bar{1}1)_{TiO2}//(\bar{2}11\bar{6})_{Cr2O3}$ interface has the strongest interfacial adhesion.

In our calculation results, the $(2\bar{1}1)_{TiO2}//(\bar{2}11\bar{6})_{Cr2O3}$ interface has the lowest interfacial energy of -33.27 eV and the largest work of adhesion of 4.48 J/m^2, meaning that TiO_2 theoretically possesses the high nucleation potency for the heterogeneous nucleation of Cr_2O_3. Therefore, it can be concluded that Cr_2O_3 is likely to preferentially nucleate and grow on the $(2\bar{1}1)$ plane of TiO_2 to form a dense and continuous Cr_2O_3 film.

4.2.2. Threshold content of Cr for a dense and continuous Cr_2O_3 film

For Fe-Cr alloys, if a dense and continuous Cr_2O_3 protective film can be formed on the surface, the critical Cr content should reach at least 20 wt.% [21]. Zhang et al. [22] argued that as the third main element in Fe-Cr alloys, Si has a large affinity with oxygen, whose oxidation could reduce the critical Cr content required for the formation of a dense and continuous Cr_2O_3 film to some degrees. However, as shown in Fig. 5, the addition of nearly 2.0 wt.% of Si could not produce a continuous Cr_2O_3 protective film on the surface of JDF1 alloy during high temperature oxidation. To quantitatively predict the critical Cr content for a protective Cr_2O_3 film on JDF alloys, the Wagner's theory [60] is used in this work, which is given by

$$N_{Cr}^{0}=\left(\frac{g_{ox}\pi}{2v}\frac{V_m}{V_{ox}}\frac{N_O^{(S)}D_O}{D_{Cr}}\right)^{\frac{1}{2}} \quad (5)$$

where g_{ox} is the oxide volume fraction and generally approximated as 0.3 [61], v is the stoichiometric coefficient of CrO_v and v=1.5 for $CrO_{1.5}$, the molar volumes of oxide V_{ox} and matrix V_m are 14.6 and 7.3 cm^3/mol, respectively, $N_O^{(S)}$ is the oxygen solubility (mole fraction) in α-Fe in equilibrium with the oxygen activity at the interface between oxide and matrix, which is taken to be 1.85×10^{-6} [57], and D_O and D_{Cr} are the diffusion coefficients of oxygen and chromium in α-Fe, respectively, which are listed in Table 4. The N_{Cr}^{0} of JDF alloys is calculated to be 0.163 (16.3 at.%), while the Cr contents in JDF alloys is about 10.9 at.%. It indicates that the actual Cr contents in JDF alloys may not theoretically lead to the formation of a continuous Cr_2O_3 film,

which is inconsistent with the observation of JDF3 in Figs. 3b, d and f.

On the other hand, in addition to the sufficient Cr content to form a protective Cr_2O_3 film, the continuous supply of Cr is also necessary to maintain the growth of Cr_2O_3 film through the Cr diffusion from the matrix to the oxide/matrix interface. In this case, the critical Cr content can be determined by [62]:

$$N_{Cr}=\frac{V_m}{32v}\left(\frac{\pi k}{D_{Cr}}\right)^{\frac{1}{2}} \quad (6)$$

$$k=\left(\frac{\Delta M}{\rho A}\right)^{n}/t \quad (7)$$

where ρ is the density of the oxide, k is the oxidation rate constant, which can be obtained by the Eq. (7) and listed in Table 6. The calculation results in Table 6 reveal that JDF1 alloy has the maximum N_{Cr} value of 0.33 while JDF3 alloy has the minimum value of 0.025. The significant reduction of N_{Cr} in JDF3 alloy may be attributed to the presence of *in situ* formed ceramic particles in the matrix. On the one hand, as mentioned in 4.2.1, the TiO_2 particles formed via the oxidation of titaniferous ceramic particles would promote the nucleation and growth of Cr_2O_3; on the other hand, NP-induced growth restriction could lead to the refinement of borides, increasing the number density of borides in the matrix [3,45] and thus facilitating the establishment of a dense and continuous Cr_2O_3 film. Therefore, compared with JDF1 alloy, a lower critical Cr content is required for JDF3 alloy in spite of almost the same Cr contents in both alloys. In this work, the D_{Cr} used to determine N_{Cr} of JDF2-4 alloys is assumed to be the same as that of JDF1 alloy due to the lack of data on D_{Cr} in JDF alloys with various particle contents. Admittedly, the *in situ* formed ceramic particles could retard the outward diffusion of Cr, leading to a smaller value of D_{Cr}. However, because the value of k in Eq. (6) is one or two orders of magnitude smaller than that of D_{Cr}, the calculation results could still show the variation trend of N_{Cr} in JDF alloys, i.e. the N_{Cr} is decreased with increasing the particle contents.

4.2.3. Adhesion of oxide scale

During the oxidation of alloys, the growth and thermal stresses would be inevitably developed in the oxide scale. Stott [63] proposed a mechanical model to determine the growth stress developed in the oxide scale, which is given by

$$\sigma_G=\frac{-E_{ox}}{1-v_{ox}}\left[(V_{ox}/V_m)^{\frac{1}{3}}-1\right] \quad (8)$$

where the elastic modulus of oxides (E_{ox}) can be obtained by Nanoindentation test,

and the Poisson's ratio (ν_{ox}) is 0.25. Because of a large difference in the thermal expansion coefficients between the matrix and the oxide, the thermal stress caused by the temperature change (ΔT) can be calculated with the following approximate expression [64]:

$$\sigma_T = \frac{-E_{ox}\Delta T(\alpha_m - \alpha_{ox})}{1-\nu_{ox}} \quad (9)$$

where σ_T is the thermal stress, α_m and α_{ox} are the thermal expansion coefficients corresponding to the matrix and oxide, respectively, α_m is about 6.85×10^{-6}/K [65] and α_{ox} is about 8.5×10^{-6}/K [66].

In this work, the critical stress can be used to evaluate the adhesion of the oxide scale, below which the growth and thermal stresses can be released via the plastic deformation of the oxide scale and above which the cracking and even the spallation of the oxide scale occur [67]. Thus, the critical stress can be defined as the maximum stress that the oxide scale can withstand without the occurrence of cracking or spallation of the oxide scale. According to Eq. (8 and 9), the calculation results of σ_G and σ_T for JDF1 and JDF3 alloys are listed in Table 7. It is shown that both the σ_G and σ_T of JDF3 alloy are larger than those of JDF1 alloy. However, different from the oxide scale of JDF1 alloy, which is rich in pores and microcracks, the oxide scale of JDF3 alloy has a thin and dense structure and is free of microcracks, showing a strong adhesion to the matrix. Therefore, it can be inferred that the critical stress of JDF3 alloy is much greater than that of JDF1 alloy.

The microstructural observation reveals that the dispersion of TiO_2 throughout the oxide scale of JDF3 alloy may be effective in enhancing the adhesion of oxide scale in two fundamental ways, one is to improve the plasticity of the oxide scale, the other is to peg the oxide scale in place. The previously formed fine TiO_2 particles may act as the heterogeneous nucleation sites for Cr_2O_3 to decrease the grain size of oxides and increase the plasticity of Cr_2O_3 scale. Furthermore, they can also induce a pegging effect to enhance the adhesion of oxide scale to the matrix, which is similar to the role of rare earth elements in improving the oxidation resistance of Cr_2O_3-forming alloys.

4.2.4. Internal depletion behavior of matrix

Fig. 11a is the SEM image of eutectic borides adjacent to the oxidation scale in JDF3 alloy after oxidation at 750 °C for 200 h. During the high temperature oxidation, the Cr-rich eutectic boride could be deemed as a source of Cr for the formation of Cr_2O_3, and thus the diffusion of Cr would generate a Boride-depleted

zone adjacent to the oxide scale. Further observation in Fig. 11b reveals that these borides are decomposed to form boride particles. In addition, a large quantity of NPs with the sizes of tens nanometers are also observed to be distributed in the matrix as displayed in the inset of Fig. 11b [3,45]. On the one hand, they can become the source of Ti for the formation of TiO_2. On the other hand, they can act as oxidation-resistant diffusion barriers to impede the outward diffusion of cations in the matrix and restrict the growth of the oxide scale. Since many NPs are consumed as the oxidation proceeds, a NP-depleted zone is formed in the proximity of the oxide scale as shown in Fig. 11c. Fig. 11d is the TEM image of the NP-depleted zone. It is found that the average size of these depleted NPs is greatly reduced to less than 10 nm. The inset of HRTEM image in Fig. 11d shows that these depleted NPs are completely coherent with the matrix. Based on the HRTEM analysis, they can be identified as the depleted TiB_2 particles. Besides, a large number of NPs are also observed to be distributed on the surface of borides. As shown in Fig. 11e, the accumulation of NPs on the surface of the primary boride results in the formation a uniform and compact NP-layer, which can not only effectively hinder the diffusion of oxygen ions into the primary boride, but also inhibit the outward diffusion of cations in the boride, thus making a great contribution to the oxidation resistance of the primary boride. Moreover, the TEM observation in Fig. 11f reveals that NPs are also distributed along the phase boundary of the eutectic boride. They either agglomerate together or aggregate forming nanochannels among them. The NP agglomeration can thoroughly stifle the diffusion of both cations and anions, whereas the nanochannels can narrow down their diffusion channel and thereby dramatically suppress their diffusion. Therefore, it can be concluded that the NPs distributed in the matrix can be effective in mitigating the internal depletion of matrix.

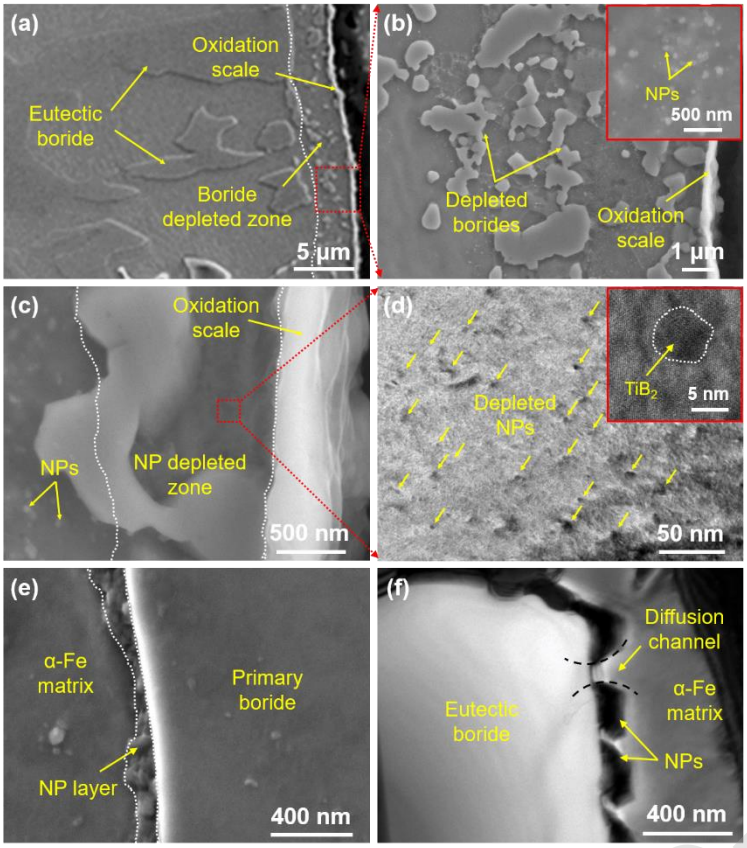

Fig. 11 Internal depletion in JDF3 alloy: (a) SEM image of the internal depleted eutectic boride; (b) SEM image of the boride depleted zone, the inset showing the NPs distributed in the matrix; (c) SEM image of the NP depleted zone; (d) TEM image showing the internal depleted NPs in the matrix, the inset is the HRTEM image of the internal depleted NPs; (e) SEM image showing the NP distributing along the interface of the primary boride; (f) TEM image showing the NP absorbing on the surface of the eutectic boride.

4.3. Oxidation behavior of NP-free conventional FeCrB alloys

Because the diffusion coefficients of B and Si in α-Fe are higher than those of Fe and Cr and the ΔG values of B_2O_3 and SiO_2 are lower than those of Cr_2O_3, Fe_2O_3 and Fe_3O_4, B_2O_3 and SiO_2 are preferentially formed on the alloy surface at the initial stage of oxidation. At the temperature of 750 °C, most of the B_2O_3 are volatilized, leaving numerous pores, which may provide the channels for the outward diffusion of Fe and Cr ions. Furthermore, the Cr content in the matrix is very limited and the formed Cr_2O_3 scale is not sufficiently dense and continuous such that it might be regarded as a short-circuit diffusion path for the outward diffusion of Fe ions and the inward diffusion of O ions, leading to the rapid formation of Fe_3O_4 oxide layer, with the

straw-like Fe_2O_3 existing in the layer. As the oxidation continues, the Fe_3O_4 oxide layer grows continuously as the oxide layer front is poor in Cr but rich in Fe. Meanwhile, driven by the inward diffusion of O ions, its reactions with Si and Cr in the matrix could generate a mixing oxide scale composed of Cr_2O_3 and SiO_2. However, such a mixing oxide scale is not dense enough to effectively inhibit the interdiffusion of alloying elements. Although a silica layer that was reported to be vitreous and taken as a diffusion barrier could be formed at the interface between the matrix and the oxide scale, the oxide scale is still susceptible to the spallation due to the absence of the pegging effect of *in situ* NPs [68,69] as shown in Fig. 5a. Therefore, JDF1 alloy exhibits a relatively poor high temperature oxidation resistance.

4.4. NP-induced anti-oxidation mechanisms in FeCrB alloys

As discussed above, due to the dispersion of titaniferous nanoparticles in the matrix, the oxidation behavior of NP-containing FeCrB alloys differs greatly from that of NP-free FeCrB alloys. Fig. 12 illustrates the anti-oxidation mechanisms of JDF alloys induced by NPs. At the initial stage of oxidation, TiO_2, SiO_2 and B_2O_3 are preferentially formed on the surface of alloys due to the low Gibbs free energy and the high diffusion coefficients in the matrix as shown in Fig. 12a. The formed B_2O_3 is extremely unstable at high temperatures and easy to volatilize, leaving some pores in the oxide layer. When Cr ions in the Cr-rich boride diffuse to the surface, the already formed TiO_2 particles can act as the heterogeneous nucleation sites for Cr_2O_3 to promote its nucleation and growth, leading to the formation of a continuous Cr_2O_3 film as depicted in Fig. 12b. The dense and continuous Cr_2O_3 film is capable of effectively inhibiting the inward diffusion of anions and the outward diffusion of cations. Because of the constant depletion of Cr, a thin oxide layer rich in Fe and Cr is formed beneath the Cr_2O_3 film (Fig. 12c). Although the amorphous SiO_2 distributed in this thin layer may fill some cavities. it is inevitable that a small amount of pores or even cavities still exist in the oxide layer, which in turn become the channels for the inward diffusion of oxygen ions. As the oxidation continues, oxygen ions that diffuse into the interface between the matrix and the oxide scale preferentially react with the NPs to form fine TiO_2 dispersions. When the chromium ions in the matrix react with oxygen ions to form Cr_2O_3 oxides, they would nucleate on the fine TiO_2 particles, producing an inner oxide layer composed of ultra-fine Cr_2O_3 as shown in Fig. 12d. The inner ultrafine-grained Cr_2O_3 layer has a dense and continuous structure and is almost free of cracks or pores. Hence, it can become an effective barrier to the

outward diffusion of cations and the inward diffusion of anions, significantly enhancing the oxidation resistance of JDF alloys.

The oxidation behavior of borides is different from that of the matrix. The NPs covering the surface of borides along with Cr-rich borides would be oxidized to form TiO_2, Cr_2O_3 as well as B_2O_3 (Fig. 12a). The Cr_2O_3 oxides can nucleate and grow on the TiO_2 (Fig. 12b), while most of B_2O_3 may be vitrified or even volatilized at high temperature. Although the volatilization of B_2O_3 might generate some pores in the layer, it can increase the activity of Cr in the borides and Si in the surrounding matrix and thus facilitate the formation of Cr_2O_3 and SiO_2. Then, SiO_2 could readily react with the residual B_2O_3 to form B_2O_3-SiO_2 borosilicate glass. During the oxidation, the Cr-rich borides may provide sufficient Cr ions for the formation of Cr_2O_3 layer as a source of Cr. As the oxidation proceeds, the outer oxide layer continues to grow and form a continuous Cr_2O_3 film (Fig. 12c). The inner Cr_2O_3 oxides mix with the borosilicate glass to form a dense and continuous inner oxide layer, further preventing the oxidation of borides as shown in Fig. 12d.

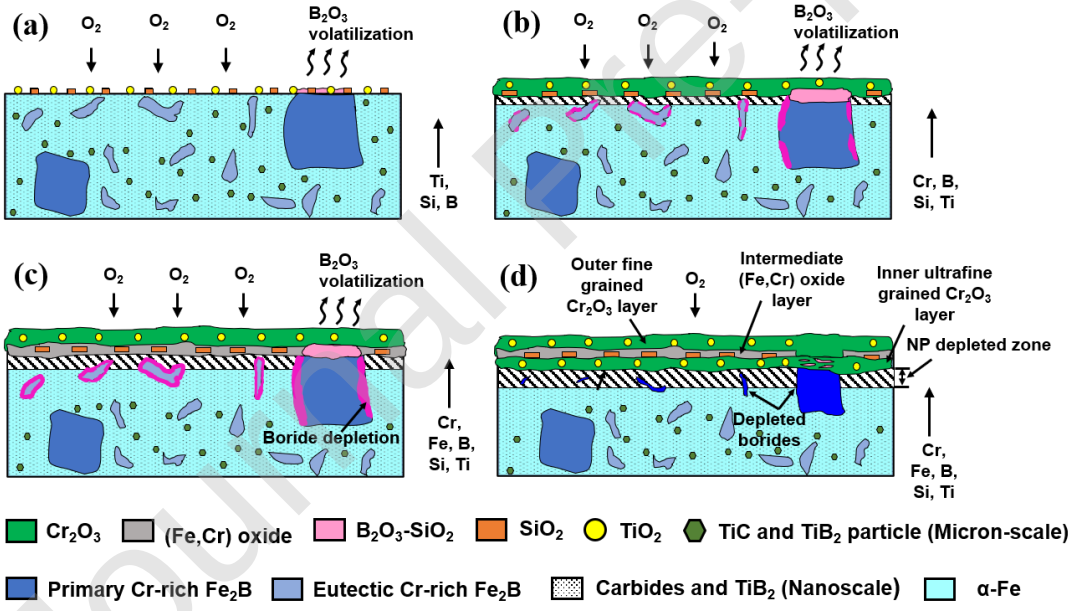

Fig. 12. Schematic diagram of the anti-oxidation mechanism for JDF alloys induced by NPs.

5. Conclusions

In this work, the surface oxide layers formed on the JDF alloys after exposure in air at 750 °C up to 200 h have been investigated by a wide range of characterization techniques. The influences of *in situ* formed NPs on the high temperature oxidation behaviors of JDF alloys have been analyzed and discussed systematically. The main

conclusions can be summarized as follows:

(1) The oxidation behavior of JDF alloys at 750 °C up to 200 h obeys a parabolic law. The NP-containing JDF alloys show more significant oxidation resistance than the NP-free JDF1 alloy, among which the JDF3 (Fe-12wt.%Cr-3.6wt.%B-1.4wt.%Ti) alloy enjoys the best oxidation resistance.

(2) Microstructural observation of JDF3 alloy demonstrates that the oxide layer formed on the α-Fe matrix can be divided into three sub-layers, i.e. the outer fine-grained Cr-rich oxide layer, the intermediate fine-grained Fe-rich oxide layer and inner ultrafine-grained Cr-rich oxide layer, while the oxide layer on the surface of primary boride can be divided into two sub-layers, i.e. the inner Cr and Si-rich layer and the outer Cr-rich layer.

(3) HRTEM analysis combined with the DFT calculation provides strong evidence that the oxidized NPs (TiO_2) formed on the surface of JDF alloys could act as the heterogeneous nucleation sites for Cr_2O_3 oxides to promote the formation of a dense and continuous Cr_2O_3 protective film that can effectively inhibit the oxidation of alloys. In addition, NPs are capable of increasing the plasticity of the oxide scale and inducing a strong pegging effect, which greatly improves the adhesion of the oxide scale to the matrix.

(4) The *in situ* NPs distributed in the α-Fe matrix can effectively inhibit the outward diffusion rate of cations in the matrix. Furthermore, the NP assembly on the surface of borides can significantly suppress the inward diffusion of oxygen ions and the outward diffusion of cations, thus making a great contribution to improving the oxidation resistance of borides. The improved oxidation resistance of both the α-Fe matrix and borides finally leads to the outstanding anti-oxidation behavior of JDF3 alloy at high temperature.

Data Availability Statement

All data included in this study are available upon request by contact with the corresponding author.

Conflict of interest

We declare that we do not have any commercial or associative interest that represents a conflict of interest in connection with the work submitted.

Author statement

Gaopeng Xu: Conceiving the concept of the research, Designing the experiments, and Writing-original draft.

Kui Wang: Conceiving the concept of the research and Writing - review & editing.

Haonan Li: Data curation.

Jiang Ju: Data curation.

Xianping Dong: Conceptualization.

Haiyan Jiang: Supervision, Project administration.

Qudong Wang: Supervision.

Wenjiang Ding: Supervision.

Acknowledgements

The present study was sponsored by the National Natural Science Foundation of China, People's Republic of China (NSFC) under Grant no. 51804197, Grant no. 51674166 and U1902220. Startup Fund for Youngman Research at SJTU (SFYR at SJTU).

References

[1] D. Balloy, J.C. Tissier, M.L. Giorgi, M. Briant, Corrosion mechanisms of steel and cast iron by molten aluminum, Metall. Mater. Trans. A 41 (2010) 2366-76.

[2] X.M. Zhang, W.P. Chen, Review on corrosion-wear resistance performance of materials in molten aluminum and its alloys, Trans. Nonferrous Met. Soc. China 25 (2015) 1715-31.

[3] G.P. Xu, K. Wang, X.P. Dong, H.Y. Jiang, Q.D. Wang, B. Ye, W.J. Ding, Multiscale corrosion-resistance mechanisms of novel ferrous alloys in dynamic aluminum melts, Corros. Sci. (2019) 108276.

[4] Z.C. Ling, W.P. Chen, T.W. Lu, B. Li, X.M. Zhang, Interfacial morphology and tribo-corrosion behaviour of Fe-15.3 wt% Cr-3.1 wt% B-6.2 wt% Mo alloy in molten aluminium, Wear 430 (2019) 81-93.

[5] S.Q. Ma, J.D. Xing, D.W. Yi, H.G. Fu, G.F. Liu, S.C. Ma, Microstructure and corrosion behavior of cast Fe-B alloys dipped into liquid zinc bath, Mater. Charact. 61

(2010) 866-872.
[6] S.Q. Ma, J.D. Xing, Y.L. He, H.G. Fu, Y.F. Li, G.Z. Liu, Effect of orientation and lamellar spacing of Fe2B on interfaces and corrosion behavior of Fe-B alloy in hot-dip galvanization, Acta Mater. 115 (2016) 392-402.
[7] S.Q. Ma, J.D. Xing, H.G. Fu, Y.L. He, Y. Bai, Y.F. Li, Y.P. Bai, Interface characteristics and corrosion behavior of oriented bulk Fe2B alloy in liquid zinc, Corros. Sci. 78 (2014) 71-80.
[8] S.Q. Ma, J.D. Xing, H.G. Fu, D.W. Yi, X.H. Zhi, Y.F. Li, Effects of boron concentration on the corrosion resistance of Fe-B alloys immersed in 460 °C molten zinc bath, Surf. Coat. Technol. 204 (2010) 2208-2014.
[9] Y. Wang, J.D. Xing, S.Q. Ma, B.C. Zheng, H.G. Fu, G.Z. Liu, Interfacial morphologies and erosion–corrosion behavior of directional Fe-3.5 wt.% B steel in flowing liquid Zn containing 0.30 wt.% Al, Corros. Sci. 112 (2016) 25-35.
[10] Y. Wang, J.D. Xing, H.G. Fu, Y.Z. Liu, K.H. Zheng, S.Q. Ma, Y.X. Jian, Interfacial morphology and corrosion-wear behavior of cast Fe-3.5 wt.% B steel in liquid zinc, Corros. Sci. 131 (2018) 290-299.
[11] X.M. Zhang, W.P. Chen, H.F. Luo, S. Li, T. Zhou, L.Y. Shi, Corrosion resistance and interfacial morphologies of novel Fe-Cr-Mo-B cast steels in molten aluminum, Corros. Sci. 125 (2017) 20-28.
[12] M.M. Wang, J. Xue, R. Gao, H.Y. Gao, Y. Zhou, Y.Y. Zhao, Y.H. Liu, M.D. Kang, J. Wang, Interface morphology and corrosion behavior of bulk Fe2B in liquid Al, Mater. Charact. 152 (2019) 1-11.
[13] D. Zhong, H. Sano, Y. Uchiyama, K. Kobayashi, Effect of low-level boron doping on oxidation behavior of polyimide-derived carbon films, Carbon 38 (2000) 1199-1206.
[14] E. Perez-Enciso, M.A. Ramos, S. Vieira, Low-temperature specific heat of different B2O3 glasses, Phys. Rev. B 56 (1997) 32.
[15] O.M. Moon, B.C. Kang, S.B. Lee, J.H. Boo, Temperature effect on structural properties of boron oxide thin films deposited by MOCVD method, Thin Solid Films 464 (2004) 164-169.
[16] Z. Lv, H.G. Fu, J.D. Xing, Z.F. Huang, S.Q. Ma, Y. Hu, Influence of boron contents on oxidation behavior and the diffusion mechanism of Fe-B based alloys at 1073 K in air, Corros. Sci. 108 (2016) 185-193.
[17] J. Ju, M.D. Kang, K.M. Wang, Y. Zhou, M. Jiang, Y.Y. Zhao, Z. Zhang, J. Wang, H.G. Fu, Studies on as-cast microstructure and oxidation behavior of the FeCrBAl

alloys at 1073 K, Vacuum, 164 (2019) 436-448.
[18]J. Ju, Chao. Yang, S.Q. Ma, M.D. Kang, K.M. Wang, J.J. Li, H.G. Fu, J. Wang, Effect of temperature on oxidation resistance and isothermal oxidation mechanism of novel wear-resistant Fe-Cr-B-Al-C-Mn-Si alloy, Corros. Sci. 170 (2020) 108620.
[19]D.P. Whittle, J. Stringer, Improvements in high temperature oxidation resistance by additions of reactive elements or oxide dispersions, Philos. Trans. R. Soc. A 295 (1980) 309-329.
[20]T.A. Ramanarayanan, M. Raghavan, R. Petkovic-Luton, The Characteristics of Alumina Scales Formed on Fe-Based Yttria-Dispersed Alloys, J. Electrochem. Soc. 131 (1984) 923.
[21]J. Stringer, The reactive element effect in high-temperature corrosion, Mater. Sci. Eng. A, 120 (1989) 129-137.
[22]L.L. Zhang, W. Yan, Q.Q. Shi, Y.F. Li, Y.Y. Shan, K. Yang, Silicon enhances high temperature oxidation resistance of SIMP steel at 700 °C, Corros. Sci. 167 (2020) 108519.
[23]T.L. Liu, K.H. Zheng, J. Wang, Y.F. Lin, Z.B. Zheng, J. Long, Effect of Ce on oxidation behaviour and microstructure evolution of a nickelsaving austenitic heat-resistant cast steel, Corros. Sci. 166 (2020) 108423.
[24]J. Lentz, A. Röttger, F. Großwendt, T. Werner, Enhancement of hardness, modulus and fracture toughness of the tetragonal (Fe,Cr)2B and orthorhombic (Cr,Fe)2B phases with addition of Cr, Mater. Des. 156 (2018) 113-124.
[25]S.Q. Ma, J.D. Xing, G.F. Liu, D.W. Yi, H.G. Fu, J.J. Zhang, Y.F. Li, Effect of chromium concentration on microstructure and properties of Fe-3.5 B alloy, Mater. Sci. Eng. A 527 (2010) 6800-6808.
[26]X.B. Liu, E. Barbero, J. Xu, M. Burris, K.M. Chang, V. Sikka, Liquid metal corrosion of 316L, Fe3Al, and FeCrSi in molten Zn-Al baths, Metall. Mater. Trans. A 36 (2005) 2049-2058.
[27]J. Stringer, Stress generation and relief in growing oxide films, Corros. Sci. 10 (1970) 513-543.
[28]Z.B. Zheng, S. Wang, J. Long, J. Wang, K.H. Zhang, Effect of rare earth elements on high temperature oxidation behaviour of austenitic steel, Corros. Sci. 164 (2020) 108359.
[29]T.A. Ramanarayanan, R. Ayer, R. Petkovic-Luton, D.P. Leta, The influence of yttrium on oxide scale growth and adherence, Oxid. Met. 29 (1988) 445-472.
[30]P.Y. Hou, J. Stringer, The effect of reactive element additions on the selective

oxidation, growth and adhesion of chromia scales, Mater. Sci. Eng. A, 202 (1995) 1-10.
[31]D.J. Sun, C.Y. Liang, E.P. Wang, H.F. Liu, X.H. Zhang, The oxidation of four oxide dispersion strengthened Ni-5Al-xSi-0.2 Y2O3 (x= 1, 3, 5, 7 wt.%) alloys in air at 1100 °C, Corros. Sci. 133 (2018) 336-348.
[32]L.L. Wei, J.H. Zheng, L.Q. Chen, R.D.K. Misra, High temperature oxidation behavior of ferritic stainless steel containing W and Ce, Corros. Sci. 142 (2018) 79-92.
[33]T.N. Rhys-Jones, H.J. Grabke, H. Kudielka, The effects of various amounts of alloyed cerium and cerium oxide on the high temperature oxidation of Fe-10Cr and Fe-20Cr alloys, Corros. Sci. 27 (1987) 49-73.
[34]X. Wei, X. Peng, X. Wang, Z. Dong, Development of growth and thermal stresses in NiO scale on nanocrystalline Ni without and with dispersion of CeO2 nanoparticles, Corros. Sci. 118 (2017) 60-68.
[35]D. Sun, C. Liang, J. Shang, J. Yin, Y. Song, W. Li, T. Liang, X. Zhang, Effect of Y2O3 contents on oxidation resistance at 1150 °C and mechanical properties at room temperature of ODS Ni-20Cr-5Al alloy, Appl. Surf. Sci. 385 (2016) 587–596.
[36]J.R. Dodson, A.J. Hunt, H.L. Parker, Y. Yang, J.H. Clark, Elemental sustainability: Towards the total recovery of scarce metals, Chem. Eng. Process. 51 (2012) 69-78.
[37]T.L. Liu, K.H. Zheng, Y.F. Lin, Z.C. Luo, Effect of second-phase particles on the oxidation behaviour of a high-manganese austenitic heat-resistant steel, Corros. Sci. 182 (2021) 109284.
[38]L. Chen, Y.Z. Sun, L. Li, X.D. Ren, Effect of heat treatment on the microstructure and high temperature oxidation behavior of TiC/Inconel 625 nanocomposites fabricated by selective laser melting, Corros. Sci. 169 (2020) 108606.
[39]Y.H. Lee, S. Ko, H. Park, D. Lee, S. Shin, I. Jo, S.B. Lee, S.K. Lee, Y. Kim, S. Cho, Effect of TiC particle size on high temperature oxidation behavior of TiC reinforced stainless steel, Appl. Surf. Sci. 480 (2019) 951-955.
[40]L. He, Y.M. Gao, Y.F. Li, Z.W. Liu, W.Y. Zhai, W. Yuan, W.Q. Chen, W.T. Yan, An effective way to solve the abnormal oxidation behavior of Fe in Ti(C,N)-304ss cermet, Corros. Sci. 155 (2019) 164-172.
[41]Q.L. Wu, J.Q. Zhang, Y.S. Sun, Oxidation behavior of TiC particle-reinforced 304 stainless steel, Corros. Sci. 52 (2010) 1003-1010.
[42]S.L. Wei, L.J. Huang, Y.T. Zhu, Z. Shi, X.T. Li, L. Geng, Sub-stoichiometry-

facilitated oxidation kinetics in a δ-TixC-doped Ti-based alloy, npj Mater. Degrad. 3 (2019) 1-5.
[43]Z. Ni, Y. Sun, F. Xue, J. Bai, Y. Lu, Microstructure and properties of austenitic stainless steel reinforced with in situ TiC particulate, Mater. Des. 32 (2011) 1462-1467.
[44]S. Cho, I. Jo, H. Kim, H.T. Kwon, S.K. Lee, S.B. Lee, Effect of TiC addition on surface oxidation behavior of SKD11 tool steel composites, Appl. Surf. Sci. 415 (2017) 155-160.
[45]G.P. Xu, K. Wang, X.P. Dong, L, Yang, H.Y. Jiang, Q.D. Wang, W.J. Ding, Effects of Titanium Addition on the Microstructural and Mechanical Property Evolution of FeCrB Alloys, Metall. Mater. Trans. A 51 (2020) 4610-4622.
[46]G.P. Xu, K. Wang, X.P. Dong, L, Yang, M. Ebrahimi, H.Y. Jiang, Q.D. Wang, W.J. Ding, Review on corrosion resistance of mild steels in liquid aluminum, J. Mater. Sci. Technol. 71 (2021) 12-22.
[47]D. Vanderbilt, Soft self-consistent pseudopotentials in a generalized eigenvalue formalism, Phys. Rev. B 41 (1990) 7892-7895.
[48]J.P. Perdew, A. Ruzsinszky, G.I. Csonka, O.A. Vydrov, G.E. Scuseria, L.A. Constantin, X. Zhou, K. Burke, Restoring the Density-Gradient Expansion for Exchange in Solids and Surfaces, Phys. Rev. Lett. 100 (2008) 136406.
[49]J.P. Perdew, K. Burke, M. Ernzerhof, Generalized gradient approximation made simple, Phys. Rev. Lett. 77 (1996) 3865-3868.
[50]B.G. Pfrommer, M. Côté, S.G. Louie, M.L. Cohen, Relaxation of crystals with the quasi-Newton method, J. Comput. Phys. 131 (1997) 233–240.
[51]T.P. Li, High Temperature Oxidation and Hot Corrosion of Metals, Chemical Industry Press, Beijing, 2003.
[52]S.H. Choi, J.S. OH, J.Y. Yun, Y.M. Kong, B.K. Kim, K.A. Lee, High temperature oxidation of Ni-Fe-Cr-Al porous metal, Adv. Eng. Mater. 15 (2013) 170-174.
[53]J.G. Duh, C.J. Wang, Formation and growth morphology of oxidation-induced ferrite layer in Fe-Mn-AI-Cr-C alloys, J. Mater. Sci. 25 (1990) 2063–2070.
[54]A.W. Bowen, G.M. Leak, Diffusion in Bcc Iron Base Alloys, Metall. Trans. 1 (1970) 2767-2773.
[55]J. Wang, S.P. Lu, L.J. Rong, D.Z. Li, Y.Y. Li, Effect of silicon on the oxidation resistance of 9 wt.% Cr heat resistance steels in 550 °C lead-bismuth eutectic, Corros. Sci. 111 (2016) 13-25.
[56]M. Keddam, S.M. Chentouf, A diffusion model for describing the bilayer growth

(FeB/Fe2B) during the iron powder-pack boriding, Appl. Surf. Sci. 252 (2005) 393-399.

[57]J. Takada, S. Yamamoto, S. Kikuchi, M. Adachi, Internal Oxidation of Fe-A1 Alloys in the α-Phase Region, Oxid. Met. 25 (1986) 93-105.

[58]B.L. Bramfitt, The effect of carbide and nitride additions on the heterogeneous nucleation behavior of liquid iron. Metall. Mater. Trans. B 1 (1970) 1987–1995.

[59]A. Arya, E.A. Carter, Structure, bonding, and adhesion at the TiC(100)/Fe(110) interface from first principles, J. Chem. Phys. 118 (2003) 8982-8996.

[60]C. Wagner, Reaktionstypen bei der oxydatoin von legierungen, Zeit Elektrochem. 63 (1959) 772-782.

[61]R.A. Rapp, The transition from internal to external oxidation and the formation of interruption bands in silver-indium alloys, Acta Metall. Mater. 9 (1961) 730-741.

[62]C. Wagner, Theoretical analysis of the diffusion processes determining the oxidation rate of alloys, J. Electrochem. Soc. 99 (1952) 369-380.

[63]F.H. Stott, A. Atkinson, The modelling of growth stresses during high temperature oxidation, Mater. High Temp. 12 (1994) 195-207.

[64]J.K. Tien, J.M. Davidson, in: J.V. Cathcart (Ed.), Stress Effects and the Oxidation of Metals Proc. TMS-aime Fall Meeting, TMS-AIME, New York, 1975, P. 200.

[65]H.Y. Tong, J.T. Wang, B.Z. Ding, H.G. Jiang, K. Lu, The structure and properties of nanocrystalline Fe78B13Si9 alloy, J. Non-Cryst. Solids150 (1992) 444-447.

[66]D.J. Young, High Temperature Oxidation and Corrosion of Metals, second ed., Elsevier Science, Amsterdam, 2016.

[67]H.E. Evans, Stress effects in high temperature oxidation of metals, Inter. Mater. Rev. 40 (1995) 1-40.

[68]D.L. Douglass, J.S. Armijo, The effect of silicon and manganese on the oxidation mechanism of Ni-20 Cr, Oxid. Met. 2 (1970) 207-231.

[69]S. Sheybany, D.L. Douglass, The effect of preoxidation on the corrosion of some superalloys in coal char, Oxid. Met. 29 (1988) 307-325.

Table 1 Chemical compositions of the JDF alloys.

Alloy	Main Chemical Compositions (wt.%)						
	C	B	Si	Cr	Ti	Ni	Fe
JDF1	0.32	3.53	1.97	11.93	-	0.49	Bal.
JDF2	0.34	3.57	1.91	12.04	0.65	0.53	Bal.
JDF3	0.33	3.60	1.95	12.17	1.37	0.51	Bal.
JDF4	0.35	3.65	1.88	11.89	2.06	0.50	Bal.

Table 2 Chemical compositions at the marked locations in Fig. 3.

Location	EDS results (at. %)				
	O	Fe	Cr	Si	Ti
1	55.48	39.30	5.22	-	-
2	62.56	35.78	1.66	-	-
3	67.42	-	-	32.58	-
4	68.12	-	-	-	31.88
5	62.67	0.75	36.58	-	-
6	58.45	1.38	40.17	-	-
7	61.96	38.04	-	-	-
8	58.73	34.43	6.83	-	-

Table 3 The ΔG and P_{O_2} for the oxidation reaction at 750 °C calculated using HSC software.

Reactions	ΔG (kJ/mol)	P_{O_2} (atm.)
$\frac{4}{3}Cr+O_2=\frac{2}{3}Cr_2O_3$	-572.6	5.8×10^{-30}
$\frac{4}{3}Fe+O_2=\frac{2}{3}Fe_2O_3$	-366.4	2.0×10^{-19}
$\frac{3}{2}Fe+O_2=\frac{1}{2}Fe_3O_4$	-385.5	2.1×10^{-20}
$\frac{4}{3}B+O_2=\frac{2}{3}B_2O_3$	-673.6	4.0×10^{-35}
$Si+O_2=SiO_2$	-726.1	8.0×10^{-38}
$Ti+O_2=TiO_2$	-760.3	1.5×10^{-39}

Table 4 Calculation of the diffusion coefficient D corresponding to different elements in α-Fe.

Elements	Cr [54]	Fe [54]	Si [55]	Ti [54]	B [56]	O [57]
Q (kJ/mol)	250.732	239.849	253.969	247.802	62.7	85.7
D_0 (m^2/s)	8.52×10^{-4}	2.0×10^{-4}	5×10^{-3}	3.15×10^{-4}	8.3×10^{-9}	2.91×10^{-7}
D (m^2/s)	1.34×10^{-16}	1.13×10^{-16}	5.38×10^{-16}	0.7×10^{-16}	5.22×10^{-12}	1.23×10^{-11}

Table 5 The calculated lattice mismatch, interfacial energy and the work of adhesion.

System	Mismatch (%)	E_{ad} (eV)	W_{ad} (J/m^2)
$TiO_2(2\bar{1}1)/Cr_2O_3(\bar{2}11\bar{6})$	4.32	-33.27	4.48
$TiO_2(020)/Cr_2O_3(11\bar{2}0)$	4.37	-13.88	2.88
$TiO_2(110)/Cr_2O_3(01\bar{1}0)$	1.65	-8.97	0.64

Table 6 Critical values of Cr content N_{Cr} of JDF alloys oxidized in air at 750 °C.

Parameters	JDF1	JDF2	JDF3	JDF4
k ($m^2\cdot s^{-1}$)	3.56×10^{-16}	1.37×10^{-17}	1.16×10^{-18}	6.51×10^{-18}
N_{Cr}	0.330	0.065	0.025	0.059

Table 7 Calculation of growth stress and thermal stress in the oxide scale.

Alloys	E_{ox} (GPa)	σ_G (GPa)	σ_T (GPa)
JDF1	31.55	10.93	0.05
JDF3	71.92	24.94	0.12